ROYAL INSTITUTE
OF TECHNOLOGY

Modelling of the radiative power loss from the plasma of the Tore Supra tokamak

Comparison of predictions from onion-skin-collisional-radiative modelling with experimental data

YUAN DING

Master Thesis

Department of Physics

Royal Institute of Technology

Stockholm, December 2008

TRITA-FYS 2008:42
ISSN 0280 – 316X
ISRN KTH/FYS/ -- 08:42 -- SE

Abstract

The one-dimensional Onion-Skin-Collisional-Radiative model is applied to Tore Supra to simulate the total radiative power loss and to study the impurity behavior (considering only carbon and oxygen) by assuming toroidal and poloidal symmetries. Under the assumption of steady state condition, ionization balance, based on collisional-radiative model, is calculated with the ionization, recombination and charge exchange rates from the ADAS database. Then, with the radiative power loss coefficients also from ADAS, the radiative power losses for all the ionization stages are assessed and summed up to give the total radiative power loss.

The validity and sensitivity to various parameters of the OSCR code are studied by a series of tests. The effective charge Z_{eff} of the plasma increases when the particle confinement time τ_p increases while the trend for the radiative power P_{rad} is opposite. The neutral hydrogen content can also play an important role in the ionization balance, since consecutive recombination from fully stripped ionization stages to lower ionization stages leads to higher radiation level. Consequently, increasing the neutral concentration leads to lower Z_{eff} and higher P_{rad}, The uncertainty in edge temperature is found to cause variations of ~5% in Z_{eff} and ~20% in P_{rad}.

The OSCR is applied to simulate pulse #39880 at Tore Supra. T_e and n_e are measured from Thomson scattering diagnostics, neutral deuterium concentration is calculated from the recycling code EDCOLL, and particle confinement time τ_p is estimated from impurity injection experiments. The total radiative power, the line-integrated brightness and the emissivity are compared with the results from the bolometers. With the input of n_C/n_e = 3% for carbon and n_O/n_e = 1% for oxygen, the total radiative power is found to be 0.34 ± 0.15 MW in agreement with the expected value 0.3MW. The brightness is found in good agreement with the experimental data; the emissivity is also in consistency with the tomographic emissivity from bolometer signal in this pulse.

Acknowledgements

First, I am very appreciated to my supervisor, Elisabeth Rachlew, for arranging the joint project between CEA-Cadarache and Atomic and Molecular Group (KTH). I got intensive instructions and helps from her after all her postgraduate students have completed their studies right before I started; moreover, her habits and attitude to science also function in educating me.

I am also grateful to Yann Corre, who also supervised me during my stay in Cadarache, for handling administrative affairs and routine life for me in the lavender season at Provence. Many thanks to him for providing the experimental data at Tore Supra and running the EDCOLL code for me. The acknowledgements are also delivered to the staffs in Cadarache for initiate my work there and providing technical data (C. Balorin, J. Lassalle and T. Aniel).

I shall not forget the warm supports and helps from Torbjörn Bäck and Janne Wallenius to my study plan and to my career.

I am also indebted to the PhD students and staffs in Reactor Physics (KTH), for assisting me in solving the problems in Matlab and LaTex *etc,* and for the family-like chats during the lunchtime.

Table of Contents

1. Introduction

This thesis is carried out as a joint project between the Atomic and Molecular Physics group, Department of Physics, Royal Institute of Technology (KTH) and CEA-Cadarache. The main objective is to adapt the Onion Skin Collisional-Radiative Model (OSCR) code, which was previously applied to Extrap-T2R at KTH, to model the impurity behavior at Tore Supra and to compare the results of the modelling with the experimental data from the bolometers installed at Tore Supra. The ADAS database is used to extract the rate coefficients for ionization, recombination, charge exchange and radiative power loss; plasma parameters, such as T_e, n_e, Z_{eff}, are taken from diagnostic measurements. With further assumptions, the total radiative power losses, considering only carbon and oxygen, are modelled within the confined plasma.

The background in fusion plasma diagnostics and radiative power loss is introduced briefly in this chapter.

1.1 Fusion reaction

Nuclear energy is the released binding energy from the strong interaction of nuclei after rearrangement in nuclear reactions; macroscopically, it is considered to be mass energy from the total weight loss of nuclei after nuclear reactions. In nuclear fusion as illustrated in Fig.1.1, two light nuclei (D, T or ^{3}He) combine (fuse) into a heavier one (plus one neutron) during which process significant mass defect energy is released.

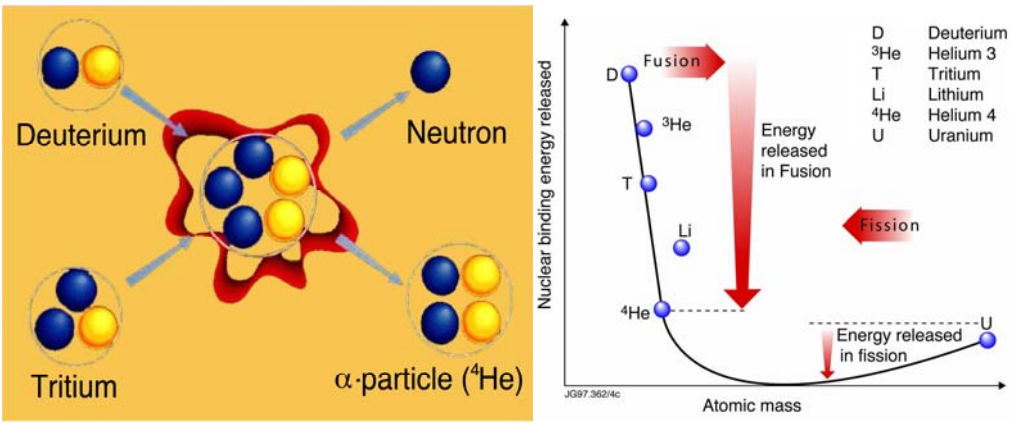

Figure 1.1 Nuclear fusion reaction (left) and binding energy as a function of atomic mass (right) ©ITER website [1]

The key issue for nuclear fusion is to squeeze the reactant nuclei as close as possible in order to overcome Coulomb repulsion and reach attractive strong force region. Thus heating of the reactant hydrogen/deuterium to 10^8 Kelvin (several 10 keV) is quite essential to reach reasonable reactivity rate. At such temperatures, the fourth state of matter: the plasma state is achieved. The controlling and heating of the plasma is the primary work to complete in order to generate fusion energy and several schemes are proposed. In this thesis, we will only work with the tokamak magnetic configuration.

1.2 Magnetic confinement-the tokamak

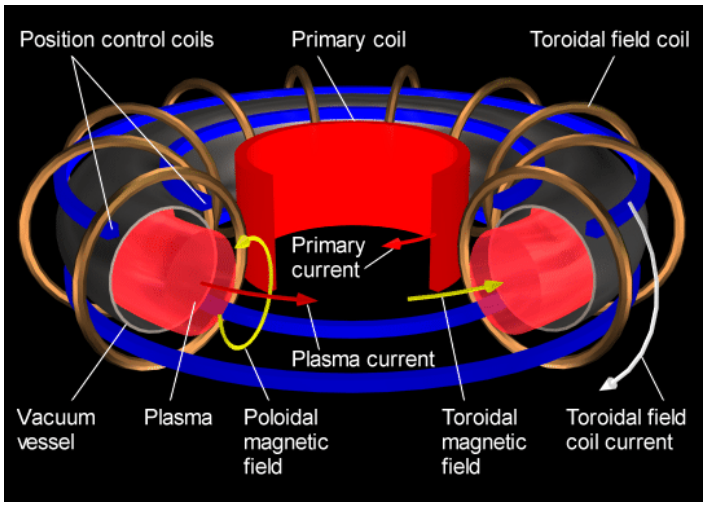

Figure 1.2 Tokamak concept: fusion fuel is contained in a vacuum vessel and confined by toroidal and poloidal magnets [2]

The tokamak was first invented by the Russians in the 1950s. Fusion fuel is contained in the torus (Fig 1.2) in which the confinement is maintained by the toroidal and current produced poloidal magnetic fields. The poloidal field compensates some particle drifts effects (mainly due to plasma curvature) to improve the plasma confinement and the toroidal field maintains the stability. The fuel can be heated to only about 3 keV [3] by Ohmic heating, as the heating efficiency is limited by the resistivity that decreases with rising temperature. Thus, additional heating mechanisms have to be exploited, *e.g.* neutral beam injection, wave heating (ion/electron cyclotron resonance heating and lower-hybrid heating *etc.*). Diagnostic instruments are installed around the torus at specially designed ports and also inside the torus with probes and coils.

The largest tokamak, ITER (International Thermonuclear Experimental Reactor), is being constructed in Cadarache, France, as a collaboration between EU, USA, Russia, China, India, Japan and South Korea, with the objective of *demonstrating scientific and technological feasibility of nuclear fusion energy for peaceful purpose* [1].

1.3 Break-even condition and radiative power loss

In a fusion device, the power balance in the plasma is formulated as [4]

$$P_{\alpha} + P_{\text{heating}} = P_{\text{rad}} + P_{\text{con}} \tag{1.1}$$

Where $P_{\alpha} \approx 20\% P_{\text{fusion}}$ is the fraction of fusion energy (defined in Eq.1.2) carried by the confined α particles to further heat the plasma; P_{heating}, P_{rad} and P_{con} are the heating power and radiative power loss and convective power loss,

Fusion energy gain factor Q is defined as the ratio of fusion power to external heating power. To reach ignition condition, it means fusion power is able to maintain the balance against any losses without external heating, Q equal to infinity is required.

The Lawson criterion is usually applied to analyze the quality of confinement and reactivity in view of reactor working operation. In this criterion, the total radiated

power (~20-30 % of input power) is usually considered simplified by only accounting bremsstrahlung radiation to estimate the criterion of ignition for fusion reactions as self-sustained system [5].

$$\eta(P_{\text{fusion}} + P_{\text{loss}} + \frac{W_{\text{store}}}{\tau_{\text{E}}}) > P_{\text{loss}} + \frac{W_{\text{store}}}{\tau_E} \tag{1.2}$$

Where $P_{\text{fusion}} = n_1 n_2 < v\sigma > E$ and $P_{\text{loss}} = \alpha n^2 T^{1/2}$, n_1, n_2 and n are the number densities of reactant 1&2 and electron density, $< v\sigma >$ is the reactivity and E is the energy released during each reaction. α is a constant, T is the electron temperature and η is efficiency of the reactor.

To estimate the ignition criterion, the power loss term is much simplified; in practical cases, the power loss can be described as composed of several processes:

- Bremsstrahlung radiation

Bremsstrahlung radiation (free-free transition) arises from the encounters of electrons with charged particles (mainly ions) due to the acceleration by the electrostatic fields. It dominates at high temperatures and its spectrum in the visible region can be extracted to calculate Z_{eff} (effective charge) with satisfactory accuracy [6].

- Recombination radiation

Apart from free-free transition by electrons, free-bound transition is the emission of a photon after the capture of an electron by an ion

$$e^- + A^z \rightarrow A^{z-1} + h\nu \tag{1.3}$$

- Line radiation

Line radiation is referred to electronic bound-bound deexcitations. It is the spontaneous emission between discrete energy states of the atoms/ions and is thus a fingerprint of the emitting ions and the states that are excited.

- Cyclotron radiation

The cyclotron movements of electrons in the magnetized plasma emit harmonic radiation of cyclotron frequency $\omega_{\text{ce}} = eB / m_{\text{e}}$ (microwave region). The resonant absorption is very strong, thus the plasma cannot be assumed to be thin in this range of wavelength. The cyclotron radiation power detected externally is low and can be neglected in the total power loss [7].

1.4 Impact of impurities

In the tokamak plasma, besides the basic fuel elements, impurity ions are present due to plasma wall interaction. The impurities can be classified into two groups:

- light impurities (C, O *etc.* normally less than 5% of the electron density in normal Tore Supra plasma operation) fully stripped at high electron temperatures, prevailing in the core of the fusion plasma
- heavy impurities (Fe, Cr, Cu, Ni *etc.* normally in small quantity during plasma operation) partly stripped and are produced by erosion from the metallic components inside the vacuum vessel [8].

The main mechanisms for production of impurities are considered to be sputtering of wall material, desorption of surface impurities, evaporation of bulk material, arcing, and chemical reactions [7,9].

The impurities pose significant impacts to fusion plasma. The main effects are fuel dilution and enhancing radiative power loss. Radiative power loss is the focus of this thesis and will only be discussed.

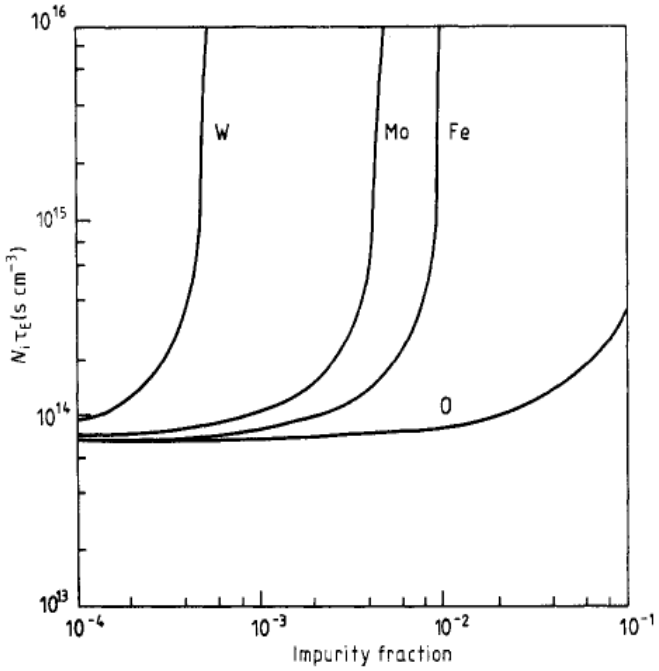

Figure 1.3 $N_i \tau_E$ requirements at break-even condition as a function of impurity levels of W, Mo, Fe and O at 10 keV [10]

As illustrated in Fig. 1.3, the requirements of break-even are significantly more stringent due to the presence of impurities, especially the heavy impurities. This is an effect of the radiation loss from the heavy impurities since they are not fully stripped and the radiation coefficients are much larger than for the lighter impurities by several orders of magnitudes due to the more complex many-electron shell structures. The presence of heavy impurities should always be minimized.

1.5 Tore Supra tokamak and its diagnostic setups

Tore Supra, located at CEA-Cadarache, France, is one of the largest tokamaks. Its superconductive toroidal magnets generate permanent toroidal magnetic field, the plasma-facing wall with heat removal system (actively cooled plasma facing component) enables long duration discharge studies. The toroidal pumped limiter is located at the bottom of the vacuum chamber. Because of recycling and erosion processes, the concentrations of low ionization stages radiations are higher near the limiter [11]. Some parameters of Tore Supra (Fig. 1.4) are given in Table 1-1.

Table 1-1 Typical parameters of Tore Supra

Major Radius (R)	2.4m
Minor Radius (a)	0.72m
Plasma Current (Max)	1.7MA
Electron Temperature (Core)	6000-7000eV
Plasma Density	0.5-10 10^{13} cm^{-3}

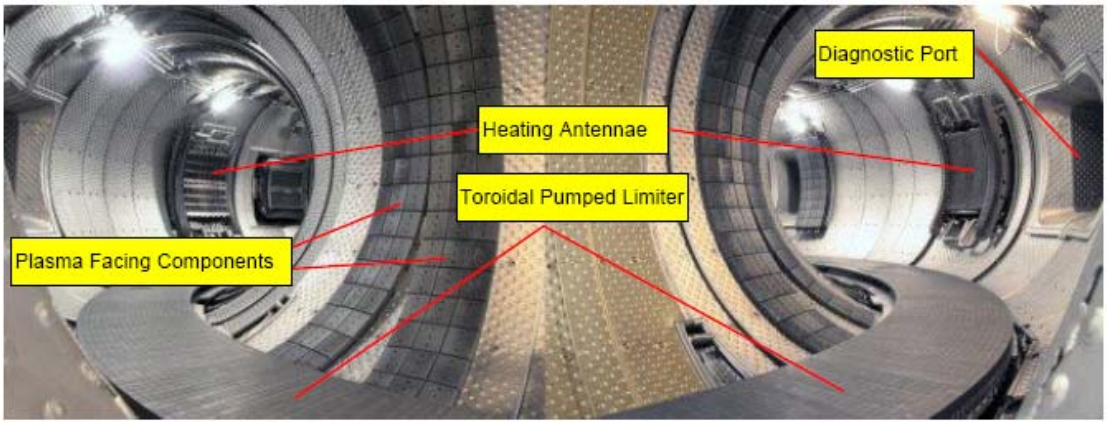

Figure 1.4 Geometry of Tore Supra R=2.4m and a=0.72 m. The toroidal pumped limiter (made of carbon fiber composite and copper alloy (CuCrZr)) is installed on the bottom of the torus, the heating antennae and diagnostic ports are located in the midplane, the block tiles made of graphite are the plasma-facing components © CEA-Cadarache

The radial profiles of electron temperature T_e and density n_e, which are input parameters for this study, are measured from twelve-channel Thomson scattering diagnostics [12]. Vacuum ultraviolet (VUV) spectrometer is installed in a midplane port to extract signals of line radiation from the impurities [13]. Furthermore, eight bolometers cover both top and side views of the torus, and measure the total radiated power with tomographing lines-of-sights [14].

1.6 Bolometers installed at Tore Supra

Metal resistor bolometers play a key role as detectors for the total radiated power in fusion devices such as ASDEX, JET, RFX and Tore Supra. The bolometer is sensitive to a wide range of radiation in VUV and soft X-ray spectrum and gives the total radiated power from the impurities [15]. The bolometers at Tore Supra (Fig.1.5) were designed by Max-Planck-Institut für Plasmaphysik (IPP) in Garching.

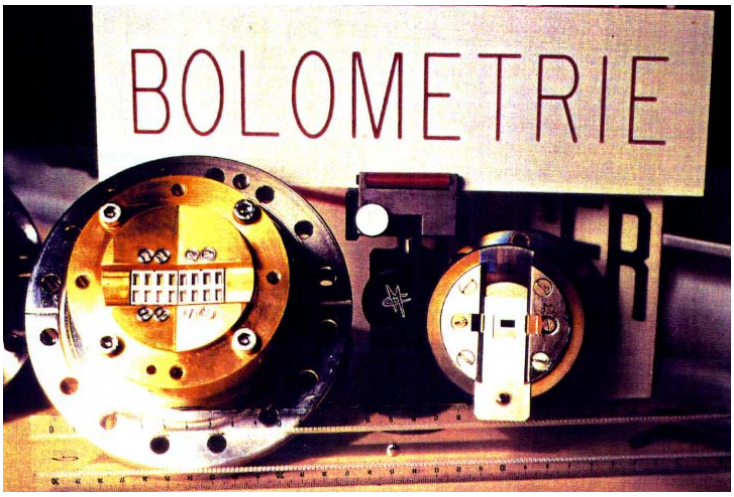

Figure 1.5 The bolometers of Tore Supra. The component on the left: eight detectors (3.8 mm*1.3 mm) are arranged symmetrically on two panels which are 5.25 degrees grazing to the normal plane of the axis, another eight are installed in parallel to form bridge circuits; the component on the right: collimating pinhole that is about 11 cm above the bolometers.

2. Ionization balance and the Onion Skin Collisional Radiative model

The detected radiative power comes mainly from the impurities *e.g.* C and O, in different ionization stages. Various atomic and radiative processes are involved, and the OSCR code is used to model the impurity behavior in order to simulate the impurity distribution and the radiative power. The result of the modelling can be compared to the bolometer or VUV signal. The details of the modelling are presented in this chapter.

2.1 Radiative and atomic processes in the plasma

In the optically thin low-density plasma, radiative power loss is equal to the sum of photon energy emitted by the plasma per unit time. In steady state ionization balance, it is proportional to the densities of electrons and ions and the radiative power loss coefficient [16].

The emitted radiation from impurities (more generally including hydrogen radiation) is normally separated into power loss due to line radiation (PLT), recombination-cascade power loss (PRR) and bremsstrahlung power loss (PBS), thus the radiative power loss (Wcm^{-3}) by a certain element is given as [17,18]

$$P_{rad} = \sum_z PZD(z) n_e n_z = \sum_z (10^{-25} \rightarrow 10^{-26}) n_e n_z \qquad (2.1)$$

Where n_e and n_z is the density (cm^{-3}) of electron and ion stages z, and PZD is the zero density radiative power coefficients (Wcm^3). The summation of the radiation from all the elements in the tokamak gives the emissivity of the plasma (total radiated power (W) after integration over the whole plasma volume, see section 2.5).

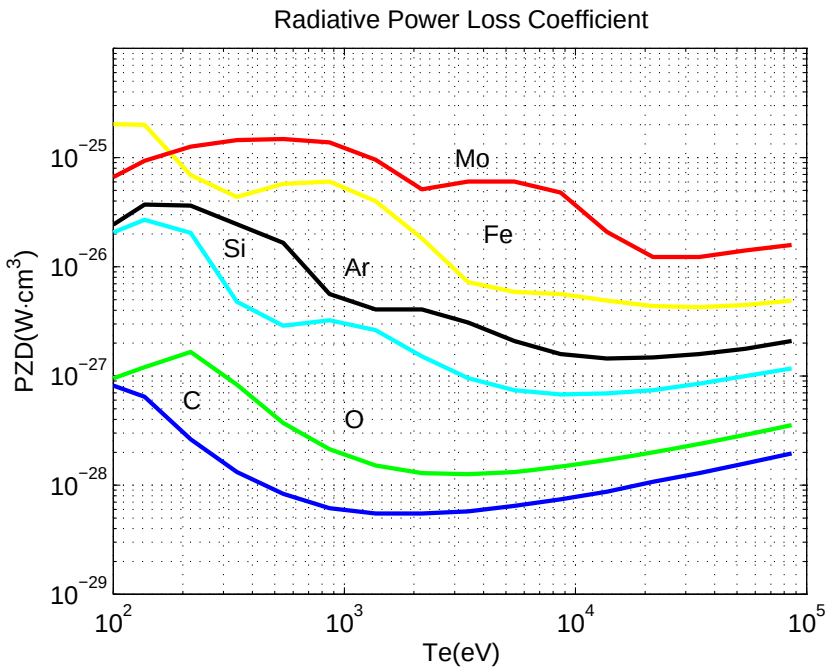

Figure 2.1 Total radiative power loss coefficients for impurities like carbon, oxygen, silicon, argon, iron and molybdenum, showing the increase with Z, constructed from ADAS [19, see Appendix].

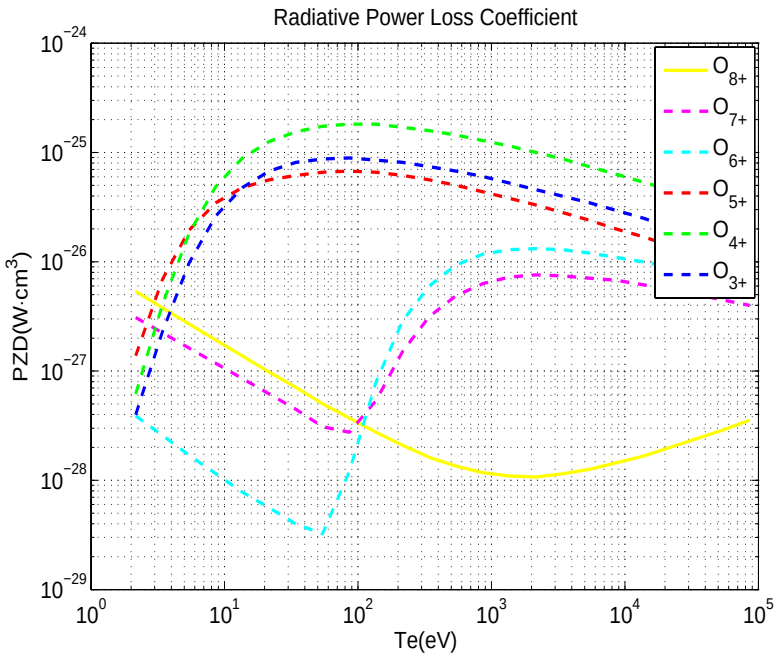

Figure 2.2 Radiative power loss coefficients for specific ionization stages of oxygen ADAS [17, 18, see Appendix]

The Z dependence of the total radiative power loss coefficients, unresolved of ion stages (under assumption ionization balance using General Collisional-Radiative Model), is illustrated by an increasing trend as shown in Fig.2.1.

- For all the impurities, an increase at high T_e is generally observed due to bremsstrahlung contribution. As an example of the radiative power loss from different ionization stages, the case for oxygen is shown in Fig.2.2 [16].
- From the curve of O^{8+}, the typical trend is shown recombination radiation is the strongest term at low T_e (when $T_e<10^3$ eV)
- For hydrogen-like ions O^{7+}, line radiation is also obvious in comparison to O^{8+}. While the same behavior even more pronounced is observed for O^{6+}, a sharp climb-up after the valley (at about 50 eV) - this can be explained by breaking the complete $1s^2$ shell structure [16,17].

In addition to the variation of the radiative power loss coefficients with T_e, the radial distribution of ions is also important in determining the total radiative power loss. The observation of the radiation is along several lines-of-sight and the modelling must integrate the radiative contributions along the lines-of-sight. Different atomic collisional processes are included but only the dominating terms are accounted for to simplify the model. The processes included are [19]:

- Electron impact ionization
- Recombination: radiative recombination (electron capture), dielectronic recombination, three body recombination
- Charge exchange recombination: the dominating process is single charge exchange with neutral atom

2.2 Ionization balance

In this work, the collisional-radiative model implemented in ADAS is used. A brief description of it is given here.

The number density of a certain ionization stage is determined by the combination of several processes [20]:

$$\begin{aligned}\frac{dn_z}{dt} &= n_{z+1}n_e\alpha_{z+1}(T_e,n_e) - n_z n_e \alpha_z(T_e,n_e) \\ &+ n_{z-1}n_e S_{z-1}(T_e,n_e) - n_z n_e S_z(T_e,n_e) \\ &+ n_{z+1}n_H C_{z+1}(T_i) - n_z n_H C_z(T_i) \\ &+ \sigma_z - \frac{n_z}{\tau_{p,z}}\end{aligned} \tag{2.2}$$

Where S_z, α_z and C_z represent the ionization, recombination and charge exchange rate coefficients, σ_z is the source term for certain ionization stages and $\tau_{p,z}$ is the particle confinement time (the z in the formula represents the initial stages of each process). Here only charge exchange with neutral hydrogen/deuterium in the ground state is included.

During the steady state of the discharge, ionization balance is assumed, and the following system of equations is solved [20]:

$$\begin{pmatrix} M_{00} & M_{10} & \cdots & M_{N0} \\ M_{01} & M_{11} & \cdots & M_{N1} \\ \vdots & \vdots & & \vdots \\ M_{0N} & M_{1N} & \cdots & M_{NN} \end{pmatrix} \cdot \begin{pmatrix} n_0 \\ n_1 \\ \vdots \\ n_N \end{pmatrix} = \begin{pmatrix} 0 \\ 0 \\ 0 \\ 0 \end{pmatrix} \tag{2.3}$$

$$M_{Z-1,Z} = n_e \cdot S_{Z-1}(T_e,n_e)$$

where $M_{Z,Z} = -n_e \cdot \alpha_Z(T_e,n_e) - n_e \cdot S_Z(T_e,n_e) - n_H \cdot C_Z(T_e,n_e) - \frac{1}{\tau_p}$

$$M_{Z+1,Z} = n_e \cdot \alpha_{Z+1}(T_e,n_e) + n_H \cdot C_{Z+1}(T_e,n_e)$$

$$M_{Z,0} = -M_{Z,1} - \frac{1}{\tau_p} \text{ when } Z \geq 1, \text{ elsewhere } M_{i,j\neq i} = 0$$

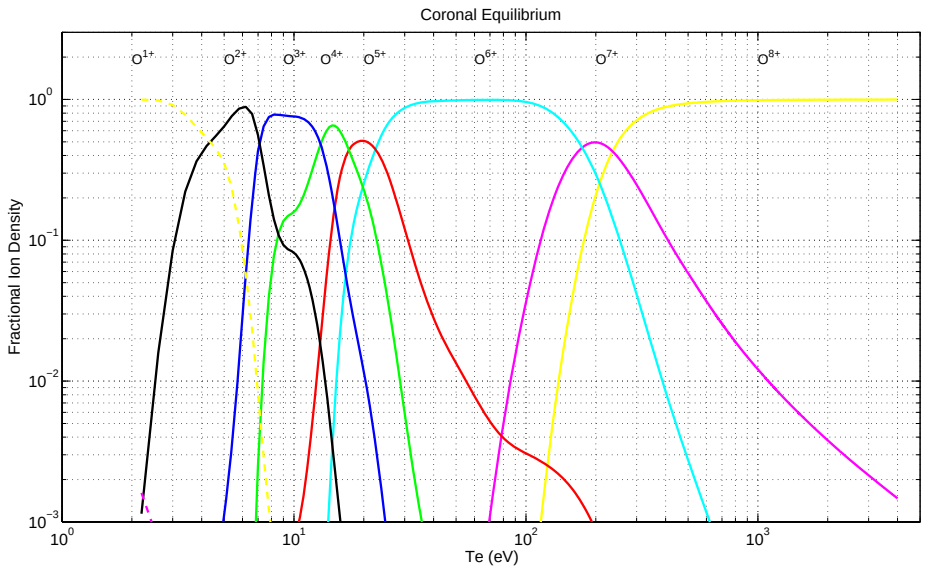

Figure 2.3 Fractional ion densities as function of T_e in coronal equilibrium

Coronal equilibrium (for the ionization distribution of oxygen is presented in Fig 2.3), neglecting charge exchange processes, source and loss term:

$$\frac{n_{z+1}}{n_z} = \frac{S_z(T_e, n_e)}{\alpha_{z+1}(T_e, n_e)} \tag{2.4}$$

2.3 The ADAS database

Atomic Data and Structure Analysis (ADAS) [18] is a set of experimental and model databases with interactive routines for extracting and analyzing populations of atoms and ions in the plasmas for interstellar, solar, fusion and industrial application. Input data of electron temperature (1-10keV) and density (10^7-10^{15}cm^{-3}) are required to extract population density.

Table 2-1 Nomenclatures

Notation	Term
SCD	Ionization rate coefficient (cm^{3}s^{-1})
ACD	Recombination rate coefficient (cm^{3}s^{-1})
TCX	Thermal charge exchange rate coefficient (cm^{3}s^{-1})
CCD	Charge exchange rate coefficient (cm^{3}s^{-1})
PLT	Line radiation power loss coefficient (Wcm^3)
PRR	Recombination power loss coefficient (Wcm^3)
PBS	Bremsstrahlung-cascade power loss coefficient (Wcm^3)
PRB	Bremsstrahlung-cascade-recombination power loss coefficient (Wcm^3)
PZD	Total power loss coefficient (Wcm^3)

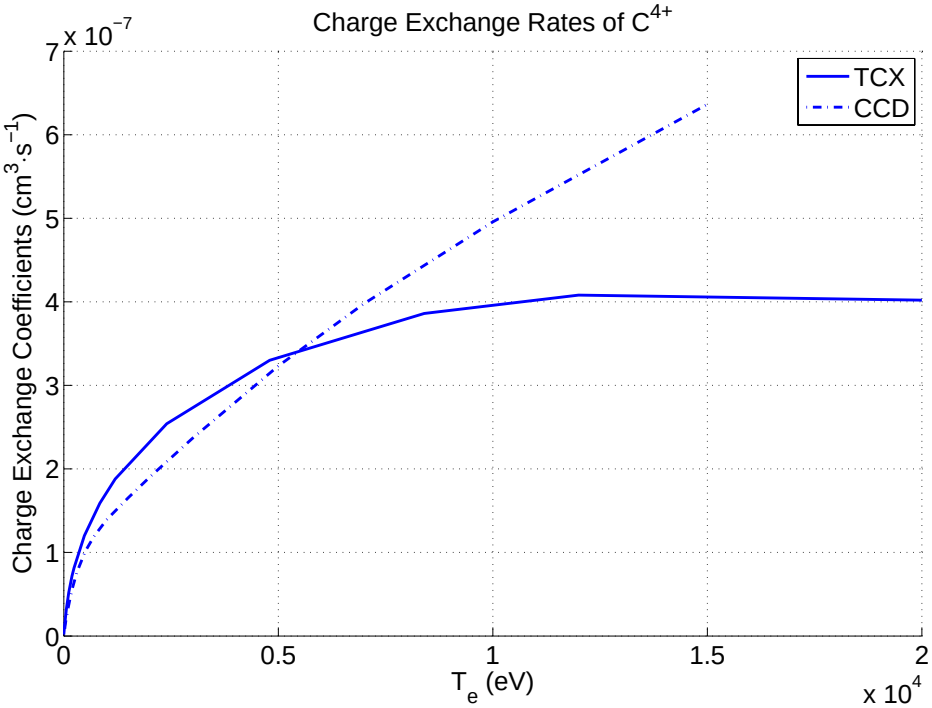

Figure 2.4 Charge exchange coefficient of C^{4+}+ D (CCD dot-dashed line, ADAS: adf11/) increases with ion temperature (T_e=T_i) monotonically, while thermal charge exchange coefficient of C^{4+}+H (TCX solid line, ADAS: adf14/) stabilizes at a constant at high T_i, but the two are still in the same order of magnitude over the temperature range of interest here (T_e < 6keV) [18, see Appendix].

Some examples of ADAS data, which appear in this study, will be introduced briefly. In general, Maxwellian distribution of electrons is assumed at local thermal equilibrium and ion temperatures are equalized to electron temperatures (this is more likely verified in the confined plasma but not any more in the scrape off layer). Some nomenclatures are tabulated in Table 2.1. CCD, which was used in the OSCR for Extrap-T2R, is charge exchange coefficient with donation from deuterium, and is replaced by TCX with neutral hydrogen as donor by setting equal ion and electron temperature under the assumption of thermal charge exchange. The two are still in the same order of magnitude and do not differ very much in relation to the uncertainties and assumptions (Fig 2.4).

2.4 The OSCR model

The Onion Skin Collisional Radiative Model [20] was applied by Y. Corre *et al.* to simulate the total radiated power of the Swedish reversed field pinch experiment (Extrap T2R) [21]. In this model, toroidal and poloidal symmetries are assumed, and only the radial dimension is considered. Due to the different physical processes near the plasma-facing wall, the scrape-off layer is excluded from the model.

Steady state ionization balance is assumed at certain duration of the discharge, with consideration of charge exchange and finite confinement. Further assumptions are made to simplify the case. Only the source term of neutral impurity atoms are considered as dominating contribution from plasma wall interaction while those of impurity ions are taken to be zero. The confinement time of neutral impurity is set to infinity, while those of different ions are assumed to be the same mainly from experimental data or scaling law [22].

$$\begin{aligned} &\sigma_0 \neq 0, \sigma_{z\neq 0} = 0 \\ &\tau_0 = \infty, \tau_{z\neq 0} = \tau_p \end{aligned} \tag{2.5}$$

In the steady state condition, for the neutrals, source and sink term can be considered in balance:

$$\sigma_0 = \frac{\sum_{z=1,N} n_z}{\tau_p} = \frac{n_{tot} - n_0}{\tau_p} \tag{2.6}$$

Solving the Eq. 2.2 with the help of Eq. 2.6 the neutral density of the impurities is given

$$n_0 = \frac{n_{tot}}{[n_e S_0 - (n_e \alpha_1 + C_1 n_H) r_{10}]\tau_p + 1} \tag{2.7}$$

Where S_0, α_1 and C_1 are the ionization rates for the neutral atom, the recombination rate and the charge exchange rate of the first ionization stage, while n_{tot} is the total number density of impurities assumed, and r_{10} is the density ratio of the first ionization stage to the neutral atoms that can be given by the rest of the equations.

Thus a restriction is posed by the coupling of the source term and the particle confinement time, as in Eq.2.6. At infinite confinement time, all the ion densities are null from Eq 2.7. So another approach is utilized in the program, since n_{tot} is also prescribed as known input.

$$n_0 = \frac{n_{tot}}{1 + r_{10} + r_{21} r_{10} + r_{32} r_{21} r_{10} \ldots + r_{N,N-1} r_{N-1,N-2} \ldots r_{21} r_{10}} \tag{2.8}$$

Several data values are included in the program and are introduced as input parameters for the program and categorized into three groups:

1. Extrapolated data: those as described in previous section 2.3, ionization (SCD), recombination (ACD), charge exchange (TCX) rates for all ionization stages, total radiative power loss coefficients (PZD), are extrapolated splinely directly or after some processing and modelling from experimental data.
2. Experimental data: the parameters that are available from the diagnostics, such as T_e, n_e. Since data points are limited, fitting with a prescribed curve are used to give finer resolution that will be described in detail in Chapter four.
3. Estimated data: some parameters in the tokamaks, *e.g.* impurity levels and their profiles, are unknown but estimated from the diagnostic results. The percentages of impurities (carbon and oxygen only) are such parameters that are not measured at Tore Supra. Z_{eff} calculated from the bremsstrahlung spectrum [6] functions as indicator to have reasonable impurity concentrations. Neutral deuterium profile is simulated with EDCOLL (Ergodic Divertor COLLetion) [23], a recycling code to estimate neutral profile.

With the input data, the distributions of various particles can be simulated. In this study, the total radiated power is investigated and compared with the detected values from the bolometer signal. The next section is the introduction of data reconstruction.

2.5 Data reconstruction

At Tore Supra, eight bolometers are installed viewing the whole cross section of the plasma, four bolometers are illustrated in Fig. 2.5 (horizontal and vertical ones are at different poloidal positions). The bolometers detect the radiative power chord-integrated along the lines of sight. Brightness (W/cm^2) is deduced from the geometry as a function of impact parameter (P) and chord angle (θ), after using tomographic reconstruction to emissivity (W/cm^3) (r-ϕ space).

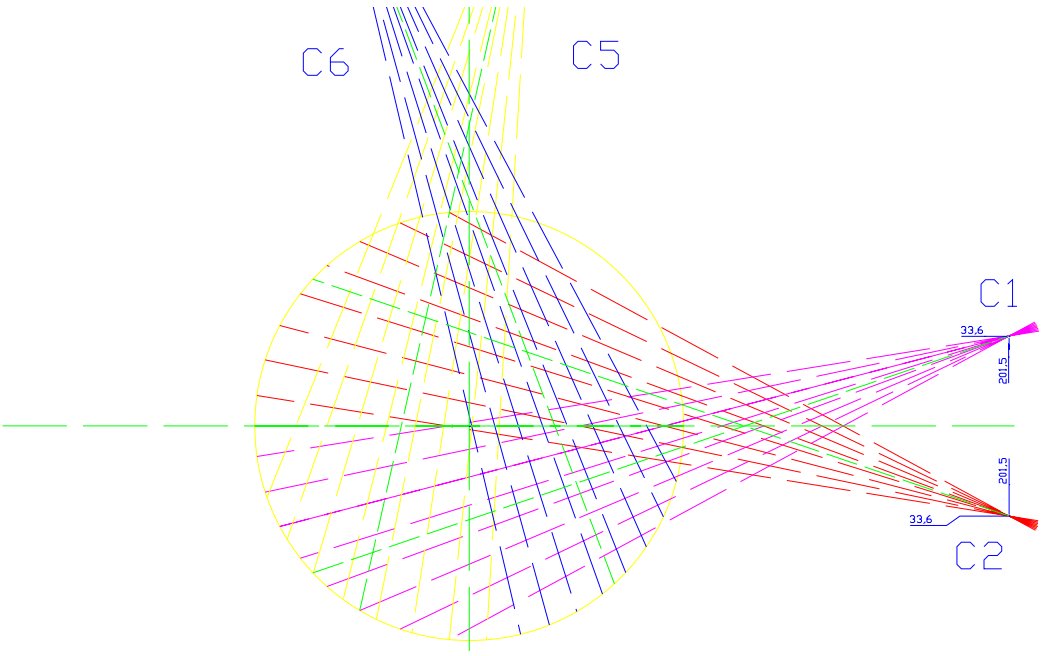

Figure 2.5 The arrays of lines-of-sights viewing the whole cross-section of the plasma, two horizontal bolometers 1&2 installed on the outboard midplane present the view over the top and bottom of the plasma and two vertical bolometer 5 &6 above the torus give the view of the inboard and outboard plasma.

As illustrated in Fig. 2.6, the volume of an infinitesimal plasma slice at the distance L from the detector is

$$\mathrm{d}V_{\mathrm{plasma}} = \frac{A_{\mathrm{ap}} \cos\theta_{\mathrm{ap}}}{d^2} L^2 dL \tag{2.9}$$

Where A_{ap} is the area of the collimating pinhole and θ_{ap} is the angle to normal plane of the line of sight, d and L are the distances from the converging point to the pinhole and to the point of integration.

The power detected from the plasma slice is limited to the solid angle viewed from the point of integration L, *i.e.* $d\Omega = A_{\mathrm{det}} \cos\theta_{\mathrm{det}} / L^2$ [24]:

$$\mathrm{d}P = \eta \frac{A_{\mathrm{det}} \cos\theta_{\mathrm{det}}}{4\pi L^2} \varepsilon \mathrm{d}V_{\mathrm{plasma}} = \eta \frac{A_{\mathrm{det}} A_{\mathrm{ap}} \cos\theta_{\mathrm{det}} \cos\theta_{\mathrm{ap}}}{4\pi d^2} \varepsilon dL \tag{2.10}$$

Where η is the average detection efficiency of the detector, A_{det} and θ_{det} are the area and angle of detector as defined for the pinhole, ε is the emissivity of the plasma *i.e.* radiative power per unit volume.

Integration along the chord gives the total power detected [24]:

$$P = \eta \frac{A_{\mathrm{det}} A_{\mathrm{ap}} \cos\theta_{\mathrm{det}} \cos\theta_{\mathrm{ap}}}{4\pi d^2} \int_{L(p,\phi)} \varepsilon(r,\theta) dL = \eta \frac{A_{\mathrm{det}} A_{\mathrm{ap}} \cos\theta_{\mathrm{det}} \cos\theta_{\mathrm{ap}}}{4\pi d^2} f(p,\phi) \tag{2.11}$$

$f(p,\phi)$ is the chord brightness, which is only function of impact parameter and chord angle, independent of the sizes, orientations of detector and pinhole.

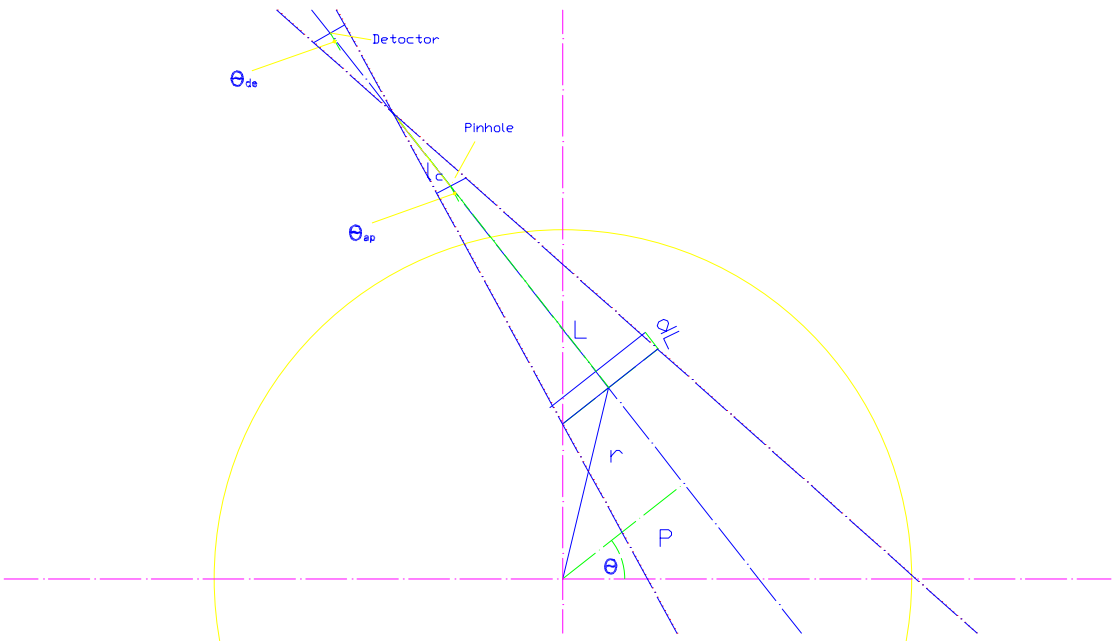

Figure 2.6 The definition of the parameters for the integration along a single line-of-sight, θ_{det} and θ_{ap} are the angles of the detector and pinhole to the normal plane of the line-of-sight, P is the impact parameter of the line-of-sight, θ is the chordal angle, r is the distance between the location of the plasma slice to the center of torus.

3. Testing of the OSCR program

After the adaptation of the OSCR program to the geometry and the range of the plasma parameters of Tore Supra, the modelling obtained with OSCR is verified by a series of tests. Furthermore, the sensitivities to various input data are also studied. Linear profiles of the electron temperature $T_e(r)$ and density $n_e(r)$ are tested in a first approximation, and the total carbon and oxygen densities are assumed as constant fraction (3%) of n_e *i.e.* the same profile but shrunk to 3%. For neutral hydrogen (hydrogen is tested in the code while deuterium is the content in the application part), linear radial rise of fraction from the core to the edge is constructed

$$\frac{n_{\mathrm{H}}(r)}{n_{\mathrm{e}}(r)} = 0.1\cdot \mathrm{f} + (\mathrm{f} - 0.1\cdot \mathrm{f})\cdot (r/\mathrm{a}) \tag{3.1}$$

where $\mathrm{f} = n_{\mathrm{H}}(a)/n_{\mathrm{e}}(a)$ is the fraction of neutral hydrogen at the edge, and is mentioned in the following text as the fraction of neutral hydrogen unless specified different. A typical input profile is shown in Fig.3.1, T_e, n_e range from 4000 eV to 2 eV and from $2.5*10^{13}$ cm^{-3} to $0.5*10^{13}$ cm^{-3}, with input of 3% C, 3% O and 10% neutral H (neutral hydrogen is not always included, but only illustrated as general case).

With input file like in Fig.3.1, the impacts of several parameters are studied: charge exchange process, particle confinement times and edge temperature. The results of these tests are presented in this chapter.

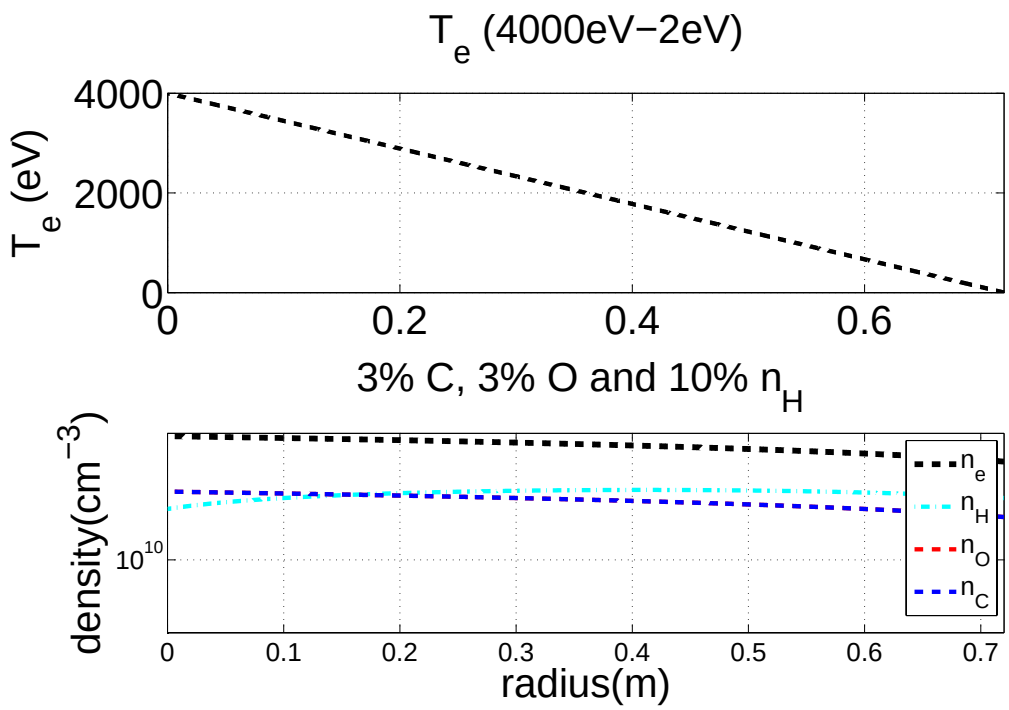

Figure 3.1 Typical input profiles for testing the program, neutral hydrogen, represented by dot dashed line, is not always included but shown as general case, oxygen and carbon, dashed lines, have the same concentration, while wider dashed line is the electron density.

3.1 Test 1: Coronal equilibrium

Coronal equilibrium assumes that excitations are caused by electron-ion collisions while deexcitations are only spontaneous emissions. The program was tested without charge exchange process and with infinite and finite particle confinement time (0.01s), to compare with coronal equilibrium (see Fig 2.3 and Fig.3.2).

Consecutive ionizations to higher ionization stages arise with increasing T_e, the correspondence with ionization energy for the shell electrons are roughly observable. A plateau is also observed for O^{6+}, which can be explained by the difficulty to ionize the closed inner shell $1s^2$.

3.2 Test 2: Impact of confinement time

The influence of particle confinement time is studied on the ionization balance, Z_{eff} and total radiated power. The ionization balance with τ_p=0.01 s is illustrated in Fig. 3.2. All the ionization stages are suppressed at lower energies and boosted at higher energies, thus the existence of non fully stripped ions at higher T_e is more probable as a general trend. As a result, Z_{eff} is reduced and the total radiative power is higher (due to the presence of more non-fully stripped ions) when τ_p decreases, as shown in Fig.3.3.

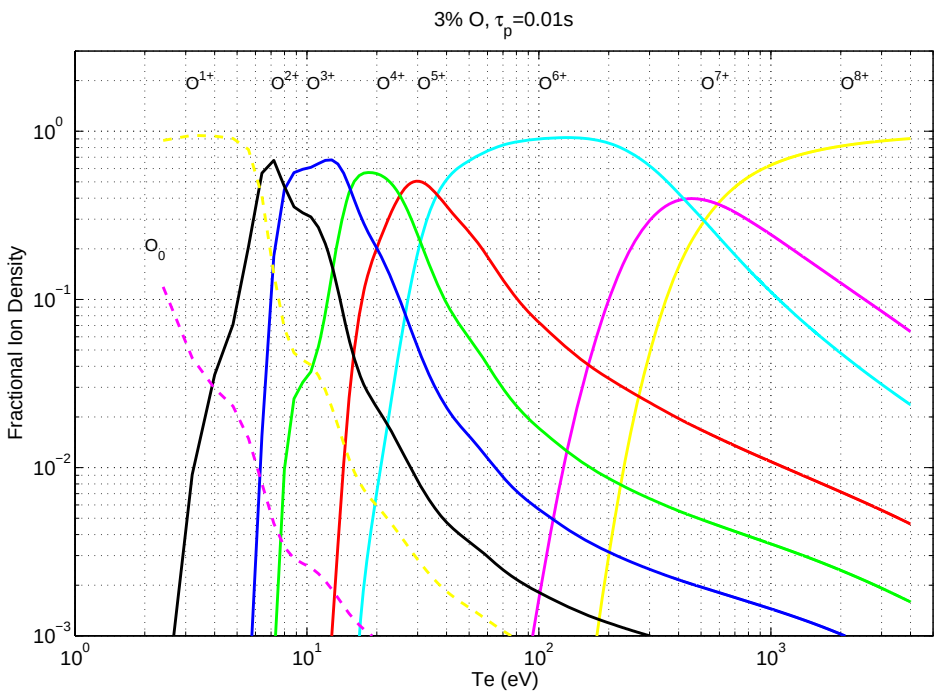

Figure 3.2 Ionization balance at τ_p=0.01s

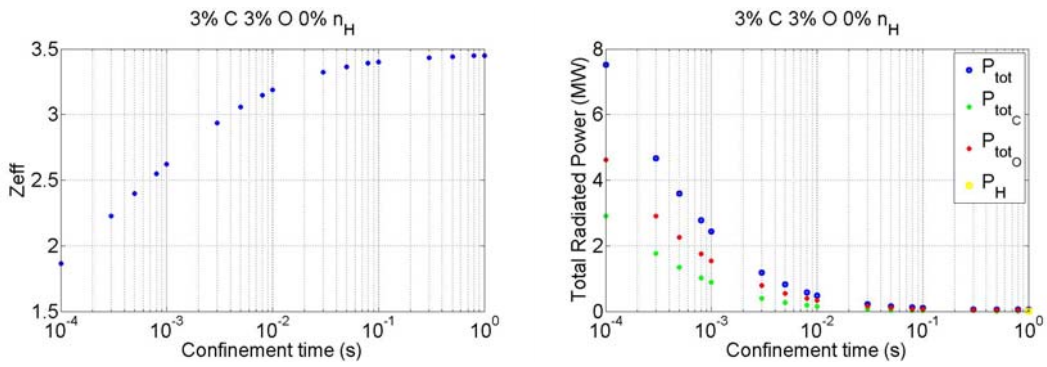

Figure 3.3 Z_{eff} (left) and P_{rad} (right) as functions of τ_p

The contributions from two main impurities (C and O) and their ionization stages are also illustrated in Fig. 3.4. Oxygen contribution to radiative power is, at the same impurity level, always larger than that from carbon by a factor of ~2. For the ionization stages, O^{7+} (hydrogen-like), O^{6+} (helium-like) and O^{8+} (bare nuclei) dominate the radiation for oxygen while C^{5+} (hydrogen-like), C^{6+} (bare nuclei), C^{4+} (helium-like) and C^{3+} (lithium-like) are the main contributors for carbon in the confinement range of interest (0.1s).

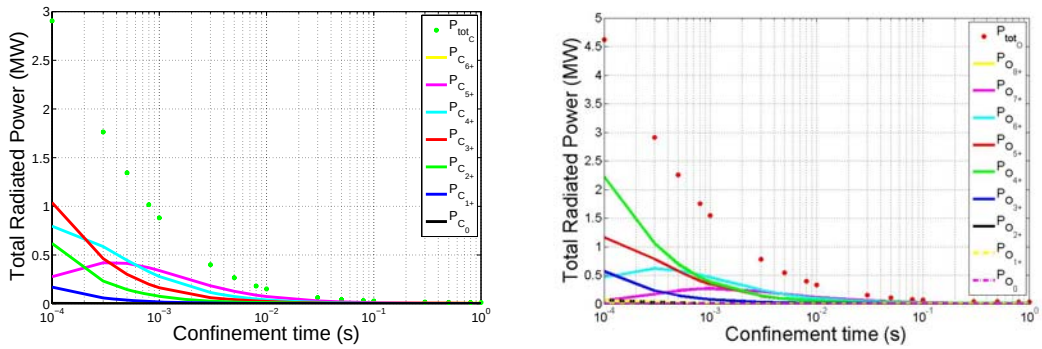

Figure 3.4 Contributions to total radiative power loss from carbon and oxygen in the different ionizations stages

3.3 Test 3: Impact of neutral hydrogen/deuterium

The charge exchange rates are normally two orders of magnitude larger than those of ionization and recombination, while the fraction of neutral hydrogen at Tore Supra is about three orders of magnitude lower than n_e, or even less, the influence is significant at neutral density of the order of 1% of n_e or more.

With the input of 1% of neutral hydrogen (constant over the whole radius in order to study its impact over T_e (T_i=T_e are assumed) only), charge exchange affects the ionization balance as the dominating recombination process, tremendous changes occur as shown in Fig. 3.5. The ions are not fully stripped ions but low ionization stages, such as O^{4+}, O^{3+}, O^{2+}, C^{3+}, C^{2+} are observed in the very hot environment.

Charge exchange recombination suppresses the average ionization stages in the ionization balance, therefore Z_{eff} decreases with increasing neutral percentage (Fig. 3.6). The impact on P_{rad} peaks at about 9%, due to the suppression to the relatively strong radiative ionization stages like O^{4+}, C^{3+} (Fig 3.7), further lower ionization

stages are not so contributing, thus a decrease is achieved with higher neutral hydrogen content.

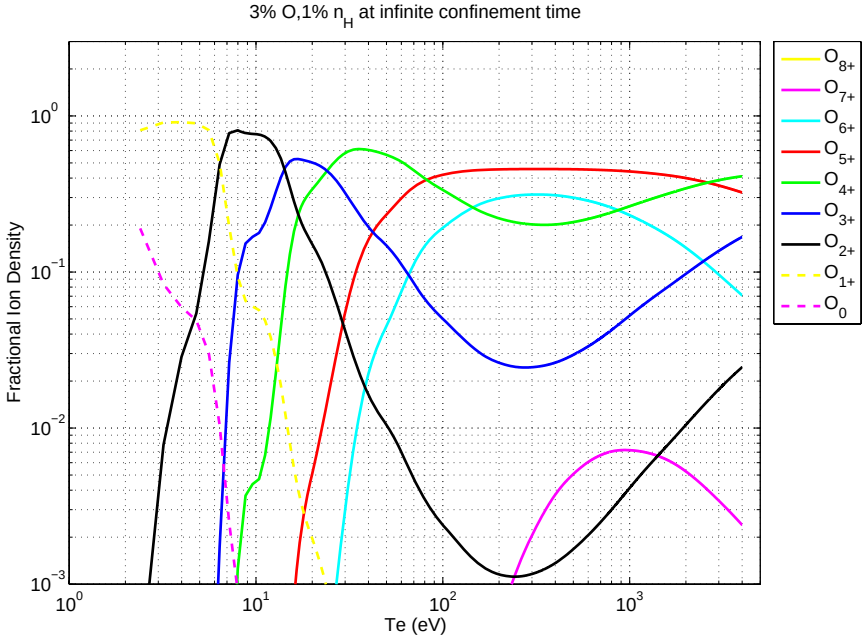

Figure 3.5 Ionization balance with 1% of neutral hydrogen

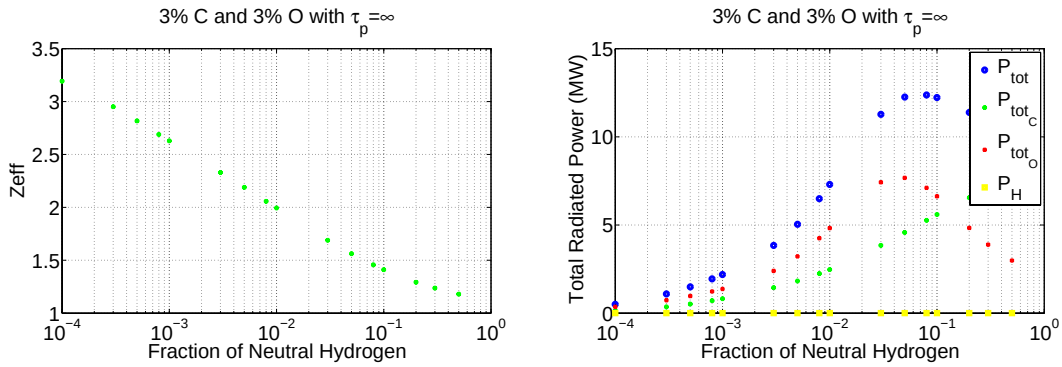

Figure 3.6 Z_{eff} decreases with the increase of the fraction of neutral hydrogen; total radiative power as a function of neutral hydrogen, the peak of the total radiated power locates at about 9% of neutral hydrogen

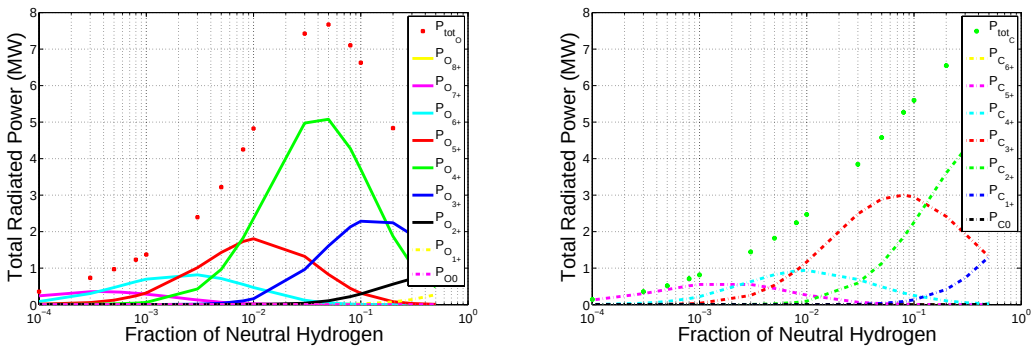

Figure 3.7 The contributions from O (left), C (right) and their ionization stages. The peak of the total radiated power locates at 5% of neutral hydrogen with O^{4+} and C^{3+} the dominating ions, while another peak due to C^{2+} is predicted at higher neutral hydrogen content.

3.4 Test 4: Impact of edge electron temperature

Edge temperature is an important parameter to the OSCR program, as it truncates directly the lower T_e part in the ionization balance scheme. Although some measurements at the scrape-off layer (SOL) are made by reciprocal Langmuir probe [25], they can only serve as lower bounds to the input values.

Several parameters are varied to study the effects of edge T_e. In the case of τ_p=0.1s, with 0% of neutral hydrogen, the impact of edge temperature on total radiated power and Z_{eff} is presented in Fig. 3.8. Z_{eff} increases slightly with rising T_e(a), by ~5% as edge T_e varies from 2 eV to 400 eV. P_{rad} is almost constant as edge T_e increases from 2-10 eV, drops ~20 % in the rise from 10-50 eV, due to the decreasing content of O^{4+}, O^{5+}, C^{3+} *etc.*, finally reduces gradually as C^{4+}, C^{5+}, O^{6+}, O^{7+} are suppressed in the range of 200-400 eV. In conclusion, the uncertainty of T_e at the edge is negligible without charge exchange.

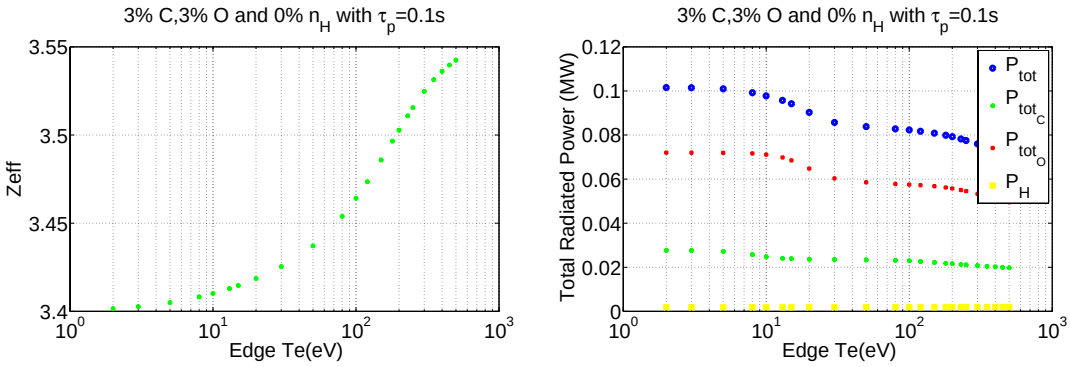

Figure 3.8 Z_{eff} (left) and P_{rad} (right) as functions of edge T_e without charge exchange

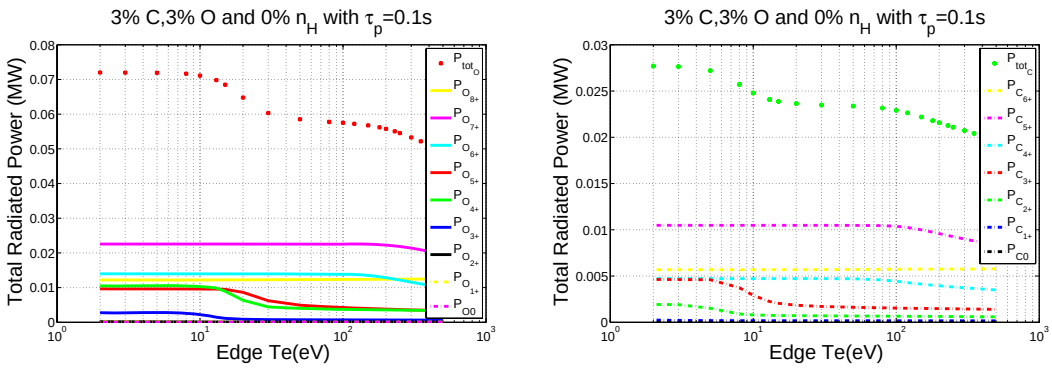

***Figure 3.9 T*he contributions from the different ionization stages of O (left) and C (right) functions of edge T_e without charge exchange**

4. Application to experimental pulse #39880

4.1 Information of pulse # 39880

The pulse # 39880 was designed to study deuterium inventory at Tore Supra [26]. Only Ohmic and lower hybrid heating were implemented (~2 MW) as total input power, the total radiated power at steady state was about 0.6 MW. It was a stable discharge, average Z_{eff} from bremsstrahlung measurement was about 2, so impurities would be low. Carbon was the dominating impurity caused by erosions from the first facing wall and divertor. The discharge was very long (120s) with low plasma current for plasma stability. Thus the long-duration and stationary pulse provided sufficiently good experimental data.

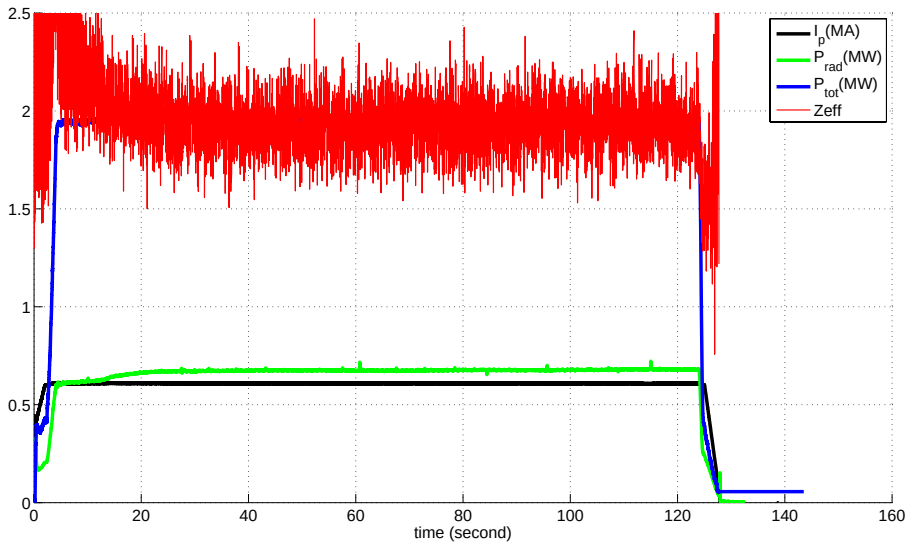

Figure 4.1 P_{tot}(MW), P_{rad}(MW), I_p (MA) and Z_{eff} as functions of time during pulse #39880, steady state was reached from about 20s to 120 s

4.2 T_e and n_e at stationary conditions

The pulse is analyzed at 35s that is assumed to be steady state. The measurement of T_e and n_e with Thomson scattering is fitted with the prescribed formulae

$$n_e(r) = n_e(a) + [n_e(0) - n_e(a)][1 - (r/a)^{\alpha}]^{\gamma} \qquad (4.1)$$

Where $n_e(0)$, $n_e(a)$ are central and edge electron densities, a is the plasma minor radius, and α and γ are parameters to be fitted. T_e has the same format but not necessarily the same parameters, T_e is bounded specifically to above 4 keV at the core and about 100 eV at the edge.

The fitted results are shown in Fig. 4.2, the core and edge T_e are fitted to be 4120 eV and 95 eV, α and γ are 2 and 3.6834, while those for n_e are $2.34*10^{13}$ cm^{-3}, $0.49*10^{13}$ cm^{-3}, 2 and 0.9486.

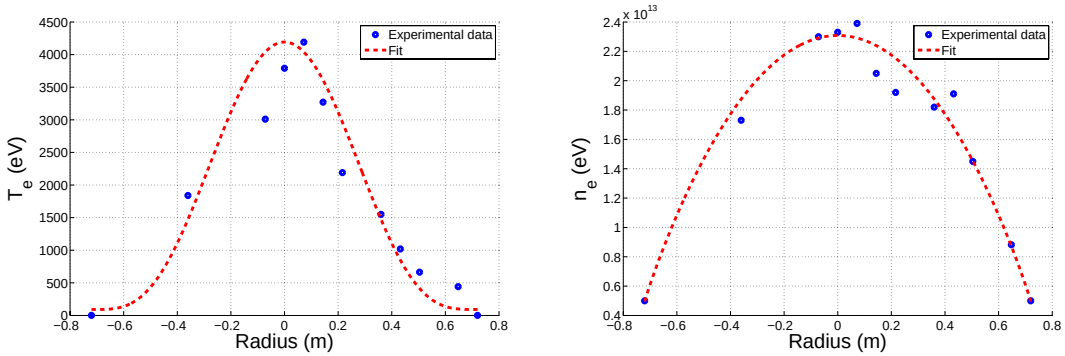

Figure 4.2 Fitting of experimental data of T_e and n_e from Thomson scattering measurements, toroidal and poloidal symmetries are assumed, the dots are experimental data, the dashed line represents the fitted curve.

4.3 Neutral deuterium radial profile

Neutral deuterium is simulated with the one-dimensional recycling code EDCOLL, which includes the following processes with plasma temperature dependence [23]:

- Dissociation of molecules and molecular ions
- Ionization
- Charge exchange

The ion influx to the wall, at steady state, is estimated with particle balance (inward and outward flux) [20]

$$<\phi_{D^+}>=\frac{\int_0^a n_e(r)\cdot 2\pi r\cdot dr}{a\cdot\tau_p} \tag{4.2}$$

Where a is the minor radius and τ_p is the particle confinement time that is the same as that of the impurities.

The input parameters are τ_p, the radial distribution of $T_e(r)$ and $n_e(r)$, including geometry of Tore Supra. Three cases are run by Y. Corre to provide radial neutral deuterium to the OSCR code as minimum (averaged deuterium influx is $<\Phi_{D+}>=3\times10^{15}$ cm^{-2}s^{-1}), reasonable ($<\Phi_{D+}>=3\times10^{15}$ cm^{-2}s^{-1}) and maximum ($<\Phi_{D+}>=3\times10^{15}$ cm^{-2}s^{-1}). The output is plotted in Fig.4.3. The ionization length of neutral deuterium is typically few centimeters, the neutral deuterium density is therefore mainly localized at the edge. It decreases by about one order of magnitude in 10 centimeters in the direction to the plasma core.

4.4 Assumption of particle confinement time

The experimental data of particle confinement time at Tore Supra can be obtained by fitting exponentially the brightness of the central chord due to soft X-ray emission from metallic impurities [12]. For the light impurities, though the C and O were not included in [12], a general τ_p is proposed to be 150 ms, which would be only in the right order of magnitude.

Another approach is to use a scaling law for Tore Supra. A simple formula fit to Tore Supra for various scenarios at different circumstances [27]:

$$\tau_p = 9.8\times10^{-6}(P_{in}/n_e)^{-0.53} \quad (4.3)$$

Where P_{in} is the input heating power (W) and n_e is the average electron density (m^{-3}), and τ_p in unit of ms. For the pulse #39880, it is calculated to be 65 ms, with P_{in}=1.95MW, n_e=1.43*10^{13}cm^{-3}.

Both of the above particle confinement times are used as input for OSCR as comparison.

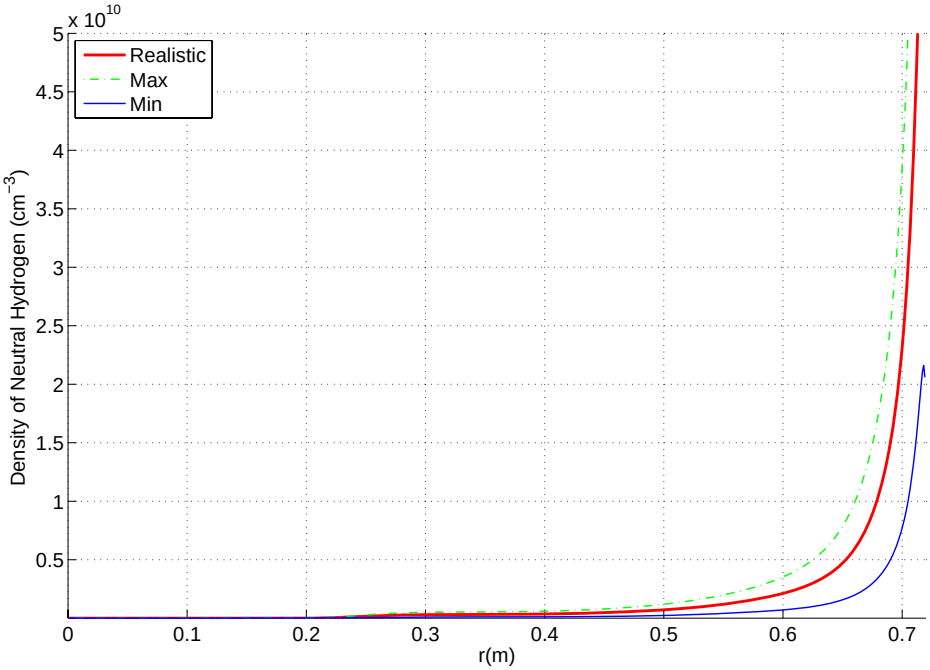

Figure 4.3 EDCOLL output neutral hydrogen profiles, wider solid line is the reasonable case, dot-dashed line and thin solid line represent the max and min cases.

4.5 Modelling of the effective charge Z_{eff} and total radiative power P_{rad}

The radiation from the plasma at Tore Supra can be divided into three regions according to [11, see Fig.4.4]:

1. Zone 1:Highly radiative region. Localized near the plasma wall interaction (*eg.* the toroidal pumped limiter) and dominated by low ionization stages. It accounts ~35% of total radiative power, but OSCR does not model this region.
2. Zone 2: Radiative layers. Quasi-symmetric region where higher ionization stages dominate, it represents ~45% of power loss.
3. Zone 3: Central plasma. Bremsstrahlung radiation of fully stripped ions is the main constituent. 25% of radiation is distributed here.

OSCR is used to model Zone 2 and 3 only. About 70% of the total radiative power (P_{rad}~0.6 MW; Fig. 4.1) belongs to Zone 2 and 3, this is equivalent to 0.42 MW. In addition, the OSCR code includes only C and O impurities. VUV measurements indicate that other impurities like Fe, Ni, Cu *etc* also contribute about 20 % of radiative power loss [28]. In conclusion, OSCR simulation should reach about 0.33 MW.

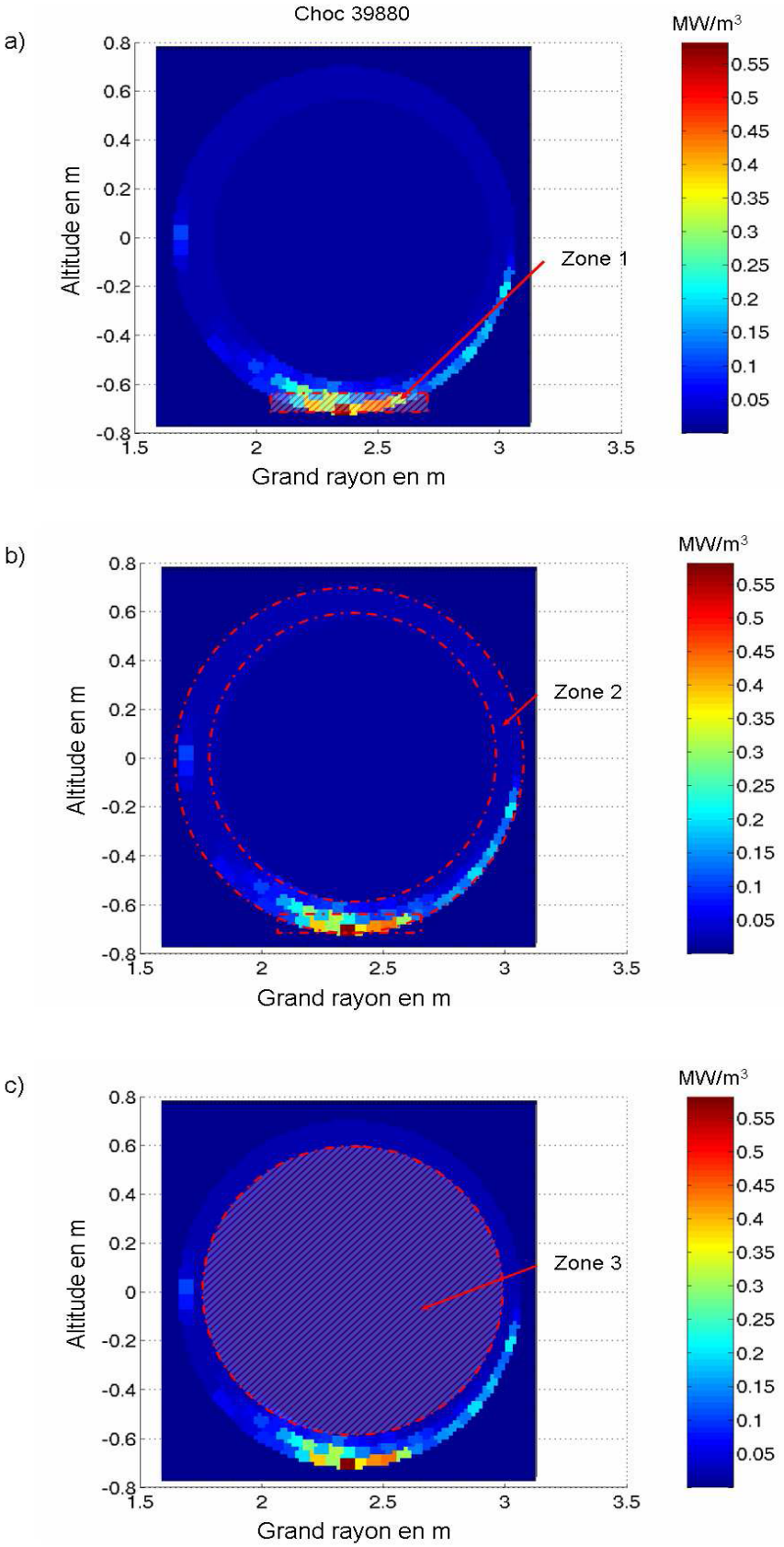

Figure 4.4 Power density distribution at: a) Zone 1; b) Zone 2; c) Zone 3, the x-axis is the major radius and y-axis is the altitude, both are in meter [11].

In order to simulate the total radiative power, Z_{eff} and P_{rad} would be matched at the same impurity level, only carbon and oxygen are considered. A constant ratio is assumed between the oxygen and carbon concentrations: total density of oxygen is 1/3 of that of carbon at pulse #39880 of Tore Supra. With the input profiles of T_e and n_e, realistic neutral deuterium density profile is adopted while max and min neutral deuterium densities serve to estimate the uncertainties. The particle confinement time is taken to be 150 ms.

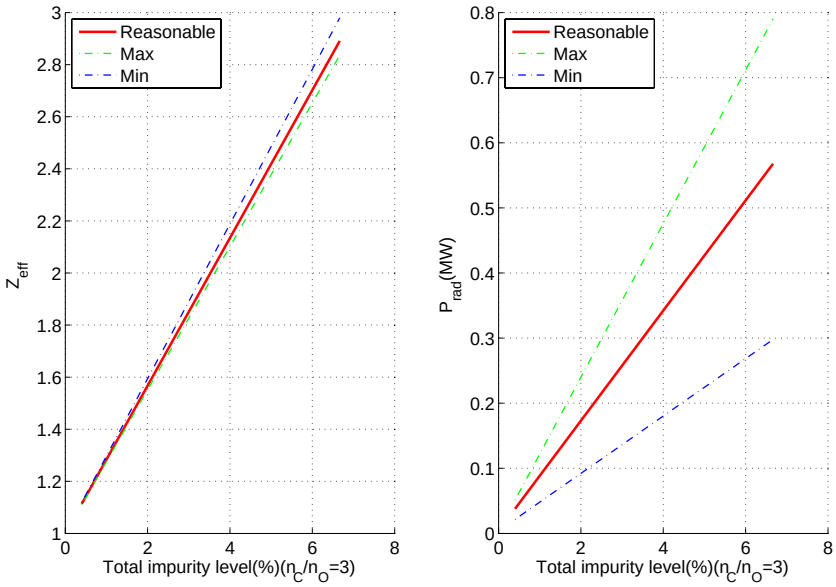

Figure 4.5 Z_{eff} and P_{rad} as functions of total impurity level (O content is 1/3 of C concentration) red line is the reasonable case, green and blue dashes represent the cases at max and min D influxes to the wall, the T_e and n_e profiles as shown in Fig.4.2 are used as input.

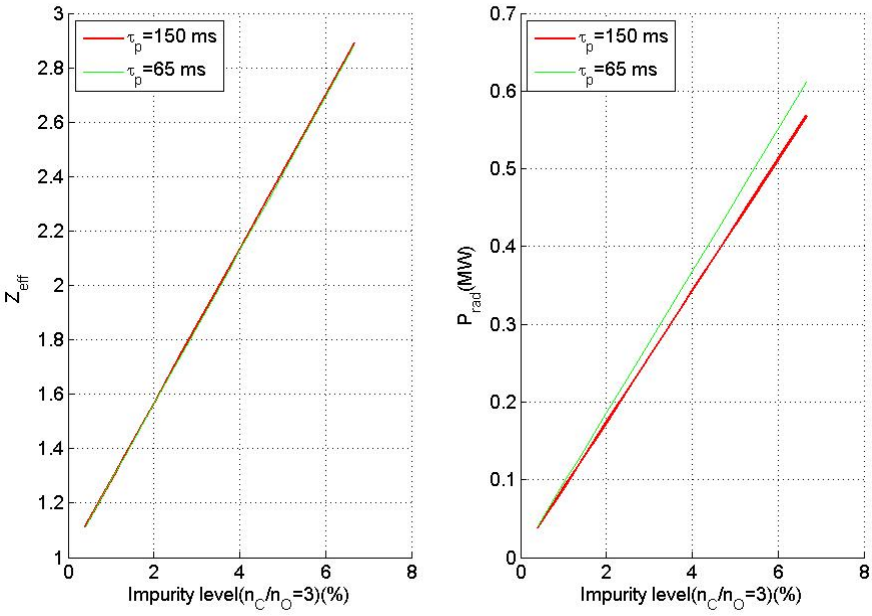

Figure 4.6 Comparison of two options of τ_p with the same input as in Fig.4.5

Z_{eff} is measured to be ~ 2 by bremsstrahlung radiation (Fig.4.1). n_C/n_e=3% (and n_O/n_e=1%), Z_{eff} is simulated to be about 2.1 as in Fig.4.5. The total radiated power P_{rad} is found to be about 0.34±0.15 MW, which is about 43% lower than the experimental value (0.6 MW) but in good agreement with the expected value 0.33MW.

A comparison is also made between two options of confinement time 150 ms and 65 ms, the impact is not significant on Z_{eff}, while a difference of ~10% is found in P_{rad}. The results of Test 2 on particle confinement time as shown in Fig.3.3 also confirm this, the influence of τ_p is very small near 100 ms, not comparable with the change caused by changes in the neutral hydrogen/deuterium concentration (see Fig.s 3.6 and 3.7). In the following sections the particle confinement time is set to 150 ms.

4.6 Chordal brightness

Based on the results of the previous section, 3% C and 1% O are adopted as input as impurities to study further other signals. The brightness as defined in Eq.2.11 is given in comparison with experimental results reconstructed from the bolometer signals in Fig.4.7.

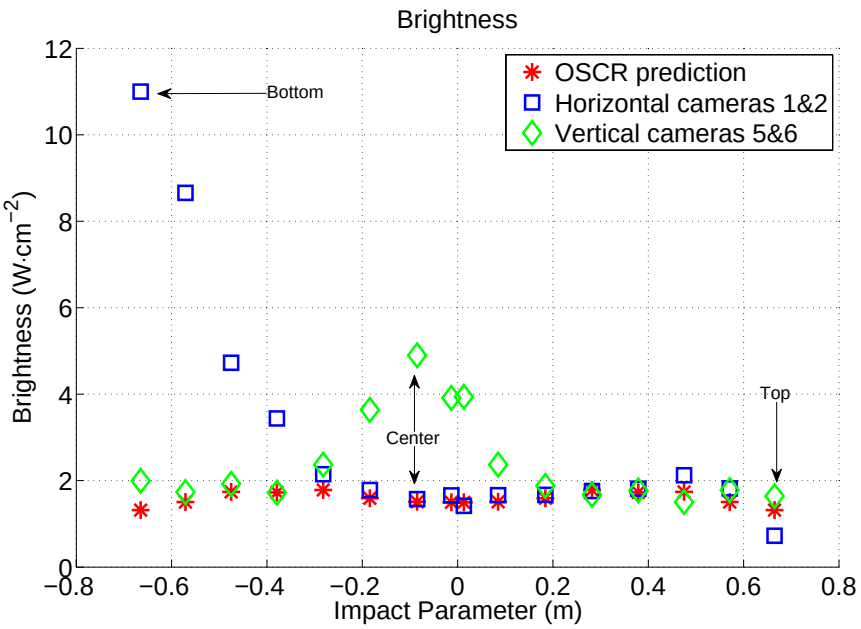

Figure 4.7 Comparison of experimental and OSCR results as functions of impact parameter (input included 3% C and 1% O, with reasonable case for neutral deuterium concentration, and τ_p=150 ms). The asterisks are OSCR prediction, the squares are the signals of horizontal cameras 1&2 and the diamonds represent the results of vertical cameras 5 &6.

The horizontal bolometers (1 and 2) are installed at midplane viewing from top of the plasma to the bottom where the toroidal pumped limiter is located; while the vertical bolometers (5 and 6) are installed at the top of the machine with views from the inboard to the outboard, as illustrated in Fig.2.5, the vertical bolometers are looking at the toroidal pumped limiter at the center. The signals of the lines-of-sight transversing the plasma near toroidal pumped limiter are stronger than from other lines-of-sight, this is due to the plasma-wall interaction (zone 1: highly radiative region). This is observed at the center of the vertical view and the bottom of the horizontal view in Fig.4.7. Since the atomic and molecular processes near the pumped

limiter are quite different from those included in our model, these parts are not considered in comparison with the OSCR results. Only the top part viewed by bolometer 2 (positive impact parameters of horizontal view) is taken to assess the modelling.

The OSCR prediction agrees well with the radiation from the region far from the limiter in the horizontal view given by bolometer 2. A little bump at about 0.4 m is observed; the brightness rises from 1.5 W/cm^2 to 1.8 W/cm^2 and reduces to 1.3 W/cm^2 at about 0.7m. A good consistency is also shown in the region covered by bolometers 5&6 far from the limiter.

4.7 Density and emissivity profiles

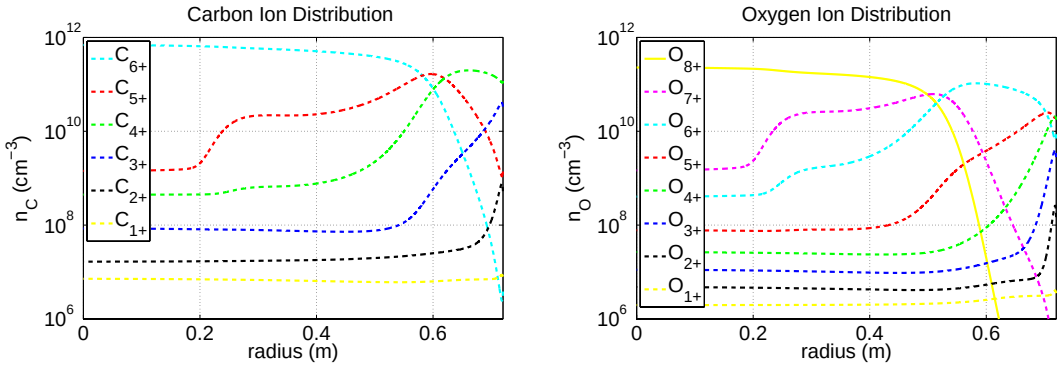

Figure 4.8 The density distribution of the main ionization stages for carbon (left) and oxygen (right) as functions of radius, with the same input profiles as in section 4.6 for pulse #39880.

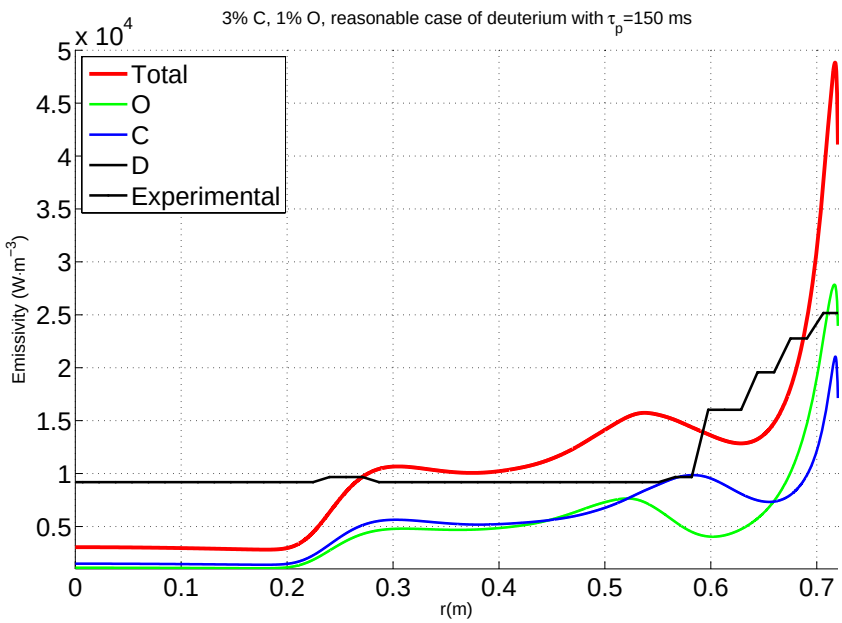

Figure 4.9 Emissivity profiles of total, carbon and oxygen radiation in comparison with the experimental data [11] (after tomographic reconstruction) with the same input as described in section 4.6, the red line is the OSCR prediction for plasma emissivity, the contributions from carbon and oxygen are represented by the blue and green lines, the black line represents the experimental emissivity.

With 3% C and 1% O, reasonable case for neutral deuterium concentration, and τ_p=150 ms, the density profiles for the ionization stages of O and C are plotted as functions of minor radius in Fig.4.8. The dominant ionization stages are summarized as follow:

Table 4-1 Dominating ionization stages at various region from the OSCR modelling

Ionization stages	Dominating region
O^{8+}	r<0.5m
O^{7+}	Near r=0.52 m
O^{6+}	0.55m < r < 0.65m
O^{5+}	Near r=0.67m
O^{4+}	r>0.7 m, near the last closed flux surface
C^{6+}	r<0.57m
C^{5+}	Near 0.6m
C^{4+}	r>0.62 m

Lower ionization stages are also present when r>0.7, but OSCR is not suitable to model them accurately

The emissivity profiles are presented in Fig.4.9. A hollow profile is predicted by OSCR in agreement with the experimental data. The strong edge region observed in the scrape-off layer (when r>0.7m) is also simulated by OSCR, but is about 2 times larger than the experimental value. Note that on one side, the spatial resolution of the bolometric signal is not suitable to measure accurately the emissivity in that region; on the other side, the OSCR is not well adapted to model radiation from low ionization stages. The comparison in the scrape-off layer is therefore difficult. There is another peak at 0.53m; this peak is mostly attributed to the helium-like (C^{4+} and O^{6+}) and also lithium-like ions (C^{3+} and O^{5+}). The plateau from 0.28m to 0.53m is attributed to the contribution from hydrogen-like ions (C^{5+} and O^{7+}) and bremsstrahlung.

5. Results and discussion

The sensitivities of the OSCR code to various input plasma parameter are studied and are concluded as follows:

- With finite particle confinement time, the general trend, in comparison with ionization balance with infinite τ_p, is that the ionization stages are shifted toward higher energy regions. Z_{eff} and P_{rad} vary significantly when τ_p < 10ms; the longer τ_p results in higher Z_{eff} and lower P_{rad}.
- Charge exchange recombination suppresses the high ionization stage population. Therefore Z_{eff} decreases when neutral hydrogen/deuterium percentage increases. A peak of P_{rad} is observed when n_H/n_e = 9%, this is attributed to the suppression to the highly radiative ionization stages like O^{4+}, C^{3+}, lower ionization stages are not so contributing.
- The uncertainties of the edge electron temperature can cause maximum uncertainty of about 20% in P_{rad} and 5% in Z_{eff} in the region of 10eV to 100 eV.

With input from diagnostic results (n_e and T_e), plus the adoption of parameters obtained in previous study (for τ_p) and a separate simulation for the neutral deuterium profile (EDCOLL for max, reasonable and min $<\Phi_{D+}>$ influxes to the wall), OSCR simulation are summarized in Table 5.1 Z_{eff} is found to be 2.10, 2.14 and 2.18, and the corresponding P_{rad} is 0.48MW, 0.34MW and 0.18 MW. So the simulated power of OSCR is still in a reasonable level (since the expected value is 0.33MW).

Table 5.1 Z_{eff} and P_{rad} at various D^+ influxes

Case	Influx ($cm^{-2}s^{-1}$)	$< n_D > / < n_e >$	Z_{eff}	P_{rad}(MW)
Maximum	$15*10^{15}$	$5.3*10^{-4}$	2.10	0.48
Reasonable	$5*10^{15}$	$3.2*10^{-4}$	2.14	0.34
Minimum	$3*10^{15}$	$1.1*10^{-4}$	2.18	0.18

Future work is required to approach the experimental results more precisely. Firstly, a better neutral deuterium profile with less uncertainty should be determined, experimentally or analytically from other diagnostic results; secondly, the impurity profiles of carbon and oxygen, or one of their ionization stages, should be studied with more reliability; a direct comparison with the VUV spectrometer data (grazing incidence VUV duochromator) is proposed in order to study the position of the radiation layers for high ionization stages. Thirdly, other impurities like W, Fe, Ni *etc.*, should also be estimated. Fourthly, if possible, make a benchmark with more codes including impurity transport (ITC code) to study the domain of validity of the OSCR simulation.

References

1. ITER website: http://www.iter.org/
2. LAP: http://www.plasma.inpe.br/LAP_Portal/LAP_Site/Text/Tokamaks.htm
3. Furth, H. P., Nucl. Fusion **15** (1975) 487
4. Johner, J., International Summer School on Fusion Technology Karlsruhe(2007) T2-3
5. Lawson, J.D. Proc. Phys. Soc. (London) **B70** (1957) 6
6. Guirlet, R., Mattioli, M., DeMichelis, C., *et al.* 21st EPS Conference on Controlled Fusion and Plasma Physics, **18B**(1994) 1280
7. Dendy, R. Plasma Physics, An Introduction Course. Cambridge University Press (1995) 432,492
8. De Michelis, C. and Mattioli, M., Rep. Prog. Phys. **47** (1984) 1233
9. Tobin, S. J., Hogan J. T., DeMichelis C., *et al.* Plasma Phys. Control. Fusion **38** (1996) 251
10. Jensen, R. V, Post, D. E., Grasberger, W. H., *et al*. Nucl. Fusion **17**(1977) 1187
11. Preynas, M., Rapport de Master 1, CEA-Cadarache (2008)
12. Parisot, T., Guirlet, R., Bourdelle, C. *et al.* Plasma Phys. Control. Fusion **50** (2008) 055010
13. De Michelis, C., Mattioli, M., Monier-Garbet, P. *et al.* Meas. Sci. Tech., **4** (1993) 109
14. Vallet, J.C., Balorin, C., Jouve, M., *et al.* 24th EPS Conference on Controlled Fusion and Plasma Physics **21A** (1997) 233
15. Mast, K. F., Vallet, J. C., Andelfinger, C., *et al.*, Rev. Sci. Instrum. **62** (1991) 744
16. Summers, H. P. and McWhirter, R. W. P., J. Phys. B. **12** (1979) 2387
17. Summers, H. P., Dickson W. J., O'Mullane M. G. *et al*., Plasma Phys. Control. Fusion **48** (2006) 263
18. ADAS : http://www.adas.ac.uk/
19. Hutchinson, I. H., Principles of Plasma Diagnostics, Cambridge Press (1987) 197
20. Corre, Y., Rachlew, E., *et al.* Physica Scripta **71** (2005) 523
21. Brunsell, P.R., Bergsåker, H., Cecconello, M., *et al.* Plasma Phys. Control. Fusion **43** (2001) 1457
22. Zastrow, K. D., PhD dissertation, Physics-KTH, Stockholm (1993)
23. Azéroual, A.,Pégourié, B., Chareyre, E. *et al.* Nucl. Fusion **40** (2000) 1651
24. Granetz, R. S., Smeulders, P., Nuclear Fusion **28**(1988) 457
25. Ledyankin, A. I., De Michelis, C., Guirlet, R. *et al.*.Phys. Lett. A **230** (1997) 209
26. Pégourié, B., Brosset, C., Tsitrone, E. *et al.* 18th Plasma Surface Interactions in Controlled Fusion Devices (2008), to be published in J. Nucl. Mater.
27. Mattioli, M., Giannella, R., Myanas, R., *et al.* Nucl. Fusion **35** (1995) 1115
28. Meyer, O., private communication.

Appendix: The ADAS data used in OSCR code

Figure 2.1

X U Total
(X represents the elements C, O, Si, Fe, Mo, Ar; U means unresolved of ionization stages)

C	adf19/pzd79/pzd93_pmw#c.dat
O	adf19/pzd79/pzd93_pmw#o.dat
Si	adf19/pzd79/pzd93_pmw#si.dat
Fe	adf19/pzd79/pzd93_pmw#fe.dat
Mo	adf19/pzd79/pzd93_pmw#mo.dat
Ar	adf19/pzd79/pzd93_pmw#ar.dat

Figure 2.2

adf19/pzd79/pzd93_pmw#o.dat

O+3	I	TOTAL	SUMMERS & MCWHIRTER(1979)
O+4	I	TOTAL	SUMMERS & MCWHIRTER(1979)
O+5	I	TOTAL	SUMMERS & MCWHIRTER(1979)
O+6	I	TOTAL	SUMMERS & MCWHIRTER(1979)
O+7	I	TOTAL	SUMMERS & MCWHIRTER(1979)
O+8	I	TOTAL	SUMMERS & MCWHIRTER(1979)

Figure 2.3 and 3.2

SCD	adf11/scd96/scd96_o.dat adf11/scd96/scd96_c.dat
ACD	adf11/acd96/acd96_o.dat adf11/acd96/acd96_c.dat

Figure 2.4

CCD	adf11/ccd89/ccd89_c.dat
TCX	adf14/tcx#h0/tcx#h0_c.dat

Other rate coefficients used in the OSCR code

SCD	adf11/scd96/scd96_o.dat adf11/scd96/scd96_c.dat
ACD	adf11/acd96/acd96_o.dat adf11/acd96/acd96_c.dat
TCX	adf14/tcx#h0/ tcx#h0_o.dat adf14/tcx#h0/ tcx#h0_c.dat
CCD Lack of O in adf11/ccd96/	adf11/ccd89/ccd89_o.dat adf11/ccd89/ccd89_c.dat
PLT	adf11/plt96/plt96_o.dat adf11/plt96/plt96_c.dat

PRB	adf11/prb96/prb96_o.dat adf11/prb96/prb96_c.dat
PZD	adf19/pzd79/pzd93_pmw#o.dat adf19/pzd79/pzd93_pmw#c.dat